Synthesis and Characterization of Infinite-Layer Nickelates in Thin Film and Bulk Form

Ishaan Singh Chandok

Due: May 5, 2022

1 Background

1.1 Experimental Background and Overview

Li et al. recently synthesized superconducting thin films of $\mathrm{Nd_{0.8}Sr_{0.2}NiO_2}$ on $\mathrm{SrTiO_3}$ substrate, and observed superconductivity at a critical temperature ($\mathrm{T_c}$) of 15 K [1]. Subsequently, the group has also showed that $\mathrm{Pr_{0.8}Sr_{0.2}NiO_2}$ films grown on $\mathrm{SrTiO_3}$ superconduct, with a $\mathrm{T_c}$ of 9 K [4]. As of today, no group has demonstrated superconductivity in either bulk sample. On the contrary, Qing et al. found evidence that $\mathrm{Nd_{0.8}Sr_{0.2}NiO_2}$ does not superconduct in bulk, and concluded that superconductivity in the thin films must be due to effects at the $\mathrm{SrTiO_3}$ interface [3]. This project aims to replicate Li et al.'s results and grow superconducting $\mathrm{Nd_{0.8}Sr_{0.2}NiO_2}$ films. As well, a second goal of the project is to use the idea of [3] and synthesize $\mathrm{Pr_{0.8}Sr_{0.2}NiO_2}$ in bulk.

Due to the discovery of high $\mathrm{T_c}$ superconductivity in cuprate compounds, researchers were curious as to whether superconductors could be made using other transition metal oxides with analogous structures. An example is $\mathrm{La_{2-2x}Sr_{2x}NiO_4}$, which is analogous to the superconducting $\mathrm{La_{2-2x}Ba_{2x}CuO_4}$. Whereas $\mathrm{La_{2-2x}Ba_{2x}CuO_4}$ is a known superconductor, with a maximum $\mathrm{T_c}$ of 30 K [10], $\mathrm{La_{2-2x}Sr_{2x}NiO_4}$ is insulating for most values of x [5]. One key difference between the undoped compounds La_2NiO_4 and La_2CuO_4 is the number of electrons in the d-orbital for Ni and Cu respectively. In La_2NiO_4, Ni takes on the d^8 state, and in La_2CuO_4, Cu takes on the d^9 state. This difference motivated the idea that to obtain a nickelate superconductor, a compound would need to be found in which the Ni ions take on the d^9 state [5].

In an attempt to obtain the d^9 configuration, as seen in high T_c cuprates, Li et al. turned to a family of compounds known as the infinite-layer (IL) nickelates [5]. With no doping, the Ni ion exhibits a formal valence of 1+, and its d orbital contains 9 electrons, much like the analogous Cu ions in the superconducting cuprates. Upon Sr doping, holes are introduced into the molecule, which makes $Nd_{0.8}Sr_{0.2}NiO_2$ a hole-doped superconductor.

The infinite-layer phase is synthesized by performing a reduction reaction on thin films of $Nd_{0.8}Sr_{0.2}NiO_3$. $Nd_{0.8}Sr_{0.2}NiO_3$ belongs to a larger family of compounds known as the Ruddlesden-Popper compounds (RP), a diagram of which can be found in [14]. In general, the formula of an RP compound is $A_{n+1}B_nO_{3n+1}$, and for $n = \infty$, it takes on the form ABO_3, which is called the perovskite phase.

The $Nd_{0.8}Sr_{0.2}NiO_3$ films are grown on $SrTiO_3$ due to the close match in their lattice parameters. As was mentioned, $Nd_{0.8}Sr_{0.2}NiO_3$ is orthorhombic, with lattice parameters of $a = 5.38$Å, $b = 5.39$Å and $c = 7.61$Å [1]. Similarily, $SrTiO_3$ is cubic, with lattice parameter $a = 3.91$Å [1]. The pseudo-cubic lattice is determined by embedding a shape that is approximately a cube inside the orthorhombic lattice of $Nd_{0.8}Sr_{0.2}NiO_3$, as in Figure 1. When $Nd_{0.8}Sr_{0.2}NiO_3$ grows on $SrTiO_3$, the ab-axis of $Nd_{0.8}Sr_{0.2}NiO_3$ rotates by approximately 45 degrees. A diagram visualizing this growth is given in Figure 2. As seen, while the lattice parameters of $Nd_{0.8}Sr_{0.2}NiO_3$ are $a = 5.38$Å and $b = 5.39$Å, the pseudo-cubic lattice parameter is $a = 3.81$Å. The pseudo-cubic lattice parameter of $Nd_{0.8}Sr_{0.2}NiO_3$ differs from $SrTiO_3$ by 2.6%, making $SrTiO_3$ a good choice as a substrate for growth.

CaH_2 reduction is used to reduce the $Nd_{0.8}Sr_{0.2}NiO_3$ films, and is visualized in Figure 3. The goal of the reduction is to remove the apical oxygens, meaning the oxygen atoms located above and below the NiO layers, from the perovskite phase. During this reduction, the perovskite $Nd_{0.8}Sr_{0.2}NiO_3$ phase transitions to the brownmillerite $Nd_{0.8}Sr_{0.2}NiO_{2.5}$ phase, and finally the

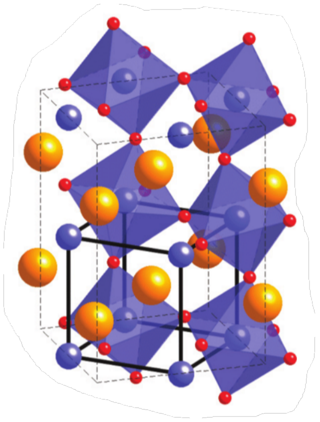

Figure 1: Orthorhombic cell of $NdNiO_3$ and corresponding pseudo-cubic unit cell. Nd atoms are orange, Ni atoms are blue and O atoms are red. Taken from [11]

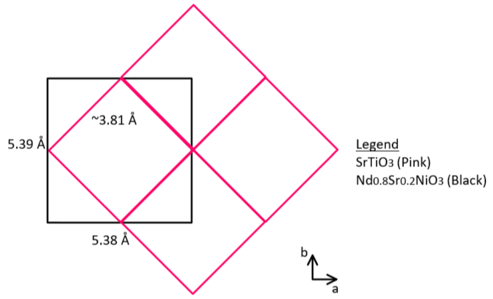

Figure 2: Growth of $Nd_{0.8}Sr_{0.2}NiO_3$ on $SrTiO_3$

infinite-layer $Nd_{0.8}Sr_{0.2}NiO_2$ phase.

1.2 Overview of Crystal Structure

A crystal is a structure made of the repetition of some unit of atoms or molecules. A crystal can be represented using a lattice and a basis, as is done in 2-dimensions in Figure 4. The lattice is an infinite set of points, where once the basis is affixed to each lattice point, returns the crystal structure.

Due to the repetitive nature of crystals, unit cells are used to simplify their structures. A unit cell is a parallelepiped spanned by three vectors a_1, a_2, and a_3, such that when infinitely repeated via translation operations, represents the entire crystal. A primitive cell is a type of unit cell with

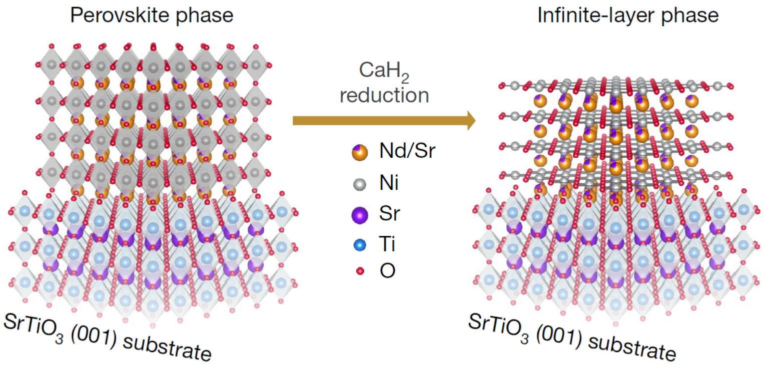

Figure 3: Reduction of Perovskite Phase to Infinite-Layer, taken from [1]

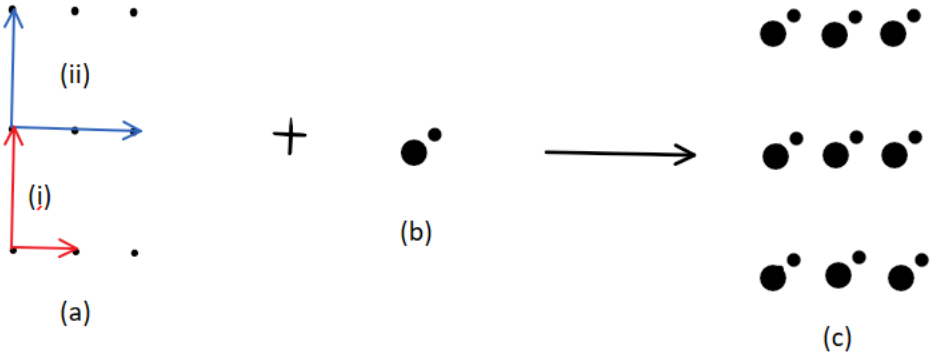

Figure 4: (a) Lattice, (b) Basis, (c) The crystal structure. Diagram based on [6].

the property that it only touches the lattice points at its vertices, and that it is the smallest cell in volume. While both parallelograms drawn on the lattice in Figure 4(a) can be used to recover the crystal structure, only (i) is a primitive cell.

The Bravais lattices refer to the family of distinct lattice types. In 3-dimensions, there are 14 Bravais lattices, listed in [6]. For example, the cubic symmetry contains 3 Bravais lattices, which are the simple cubic (sc), body-centred cubic (bcc) and face-centred cubic (fcc). Often Bravais lattices are represented via non-primitive (conventional) cells instead of primitive cells, as the non-primitive cells better display the symmetry properties of the crystal. A table of structures important to this experiment is as follows.

Compound	Crystal Structure	Lattice Parameters
NiO	Cubic	a = 4.17Å
$SrTiO_3$	Cubic	a = 3.91Å
$Nd_{0.8}Sr_{0.2}NiO_3$ (bulk)	Orthorhombic	a = 5.38Å, b = 5.39Å, c = 7.61Å
$Nd_{1.6}Sr_{0.4}NiO_4$ (bulk)	Orthorhombic	a = 5.37Å, b = 5.45Å, c = 12.36Å

The Miller index is three integers used to represent the orientation of a plane or family of planes with respect to the unit cell of a crystal. The plane P_{hkl} with Miller index (hkl) is defined as the plane intersecting the unit cell at $(\frac{a_1}{h}, \frac{a_2}{k}, \frac{a_3}{l})$. The family of planes with index (hkl), denoted $\mathcal{P}_{hkl}$, is obtained by first finding the plane P'_{hkl} that intersects the origin and is parallel to P_{hkl}. Then, $\mathcal{P}_{hkl}$ is defined as the collection of planes parallel to P_{hkl} and with interplanar spacing equal to the distance between P_{hkl} and P'_{hkl}. The separation of these planes is denoted d_{hkl}. The plane and family of planes with Miller index (002) is drawn in Figure 5.

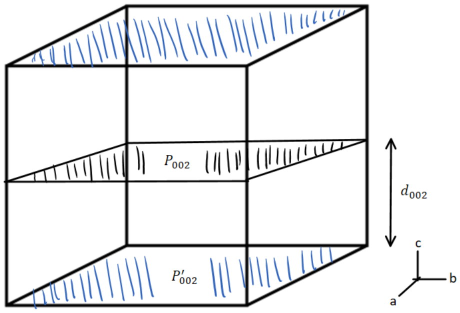

Figure 5: The family of planes $\mathcal{P}_{002}$

The formula for d_{hkl} can be deduced by considering the geometry of each Bravais lattice. For example, for the cubic family of lattices with lattice parameter a,

$$d_{hkl} = \frac{a}{\sqrt{h^2 + k^2 + l^2}}$$

Crystals have a theoretical density, which is a measure of the largest density a crystal structure can attain under perfect packing. It is given by the mass of the crystal divided by its volume, and can be written as

$$\rho = \frac{\mathrm{ZM_w}}{\mathrm{V_c N_a}}$$

Where Z is the number of atoms/molecules per unit cell, $\mathrm{M_w}$ is the atomic/molecular weight, $\mathrm{V_c}$ is the cell volume and $\mathrm{N_a}$ is Avagadro's constant. In this paper, the theoretical density of NiO and $\mathrm{Nd_{1.6}Sr_{0.4}NiO_4}$ are needed.

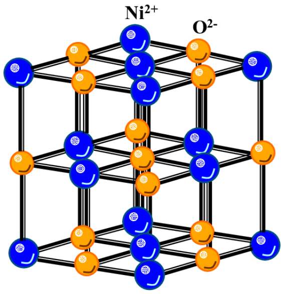

Figure 6: Structure of NiO. Ni atoms are blue and O atoms are orange. Taken from [12].

NiO is a crystal with the face-centred cubic structure, and its unit cell is drawn in Figure 6. As seen, there are 4 NiO molecules per cell, so the theoretical density is

$$\rho_{\mathrm{NiO}} = \frac{(4)(58.69\mathrm{g/mol} + 16.00\mathrm{g/mol})}{((4.17 \times 10^{-8}\mathrm{cm})^3 * (6.02 \times 10^{23}\frac{1}{\mathrm{mol}}))} = 6.84\frac{\mathrm{g}}{\mathrm{cm}^3}$$

A similar calculation shows that the theoretical density of $\mathrm{Nd_{1.6}Sr_{0.4}NiO_4}$ is $7.26\frac{\mathrm{g}}{\mathrm{cm}^3}$.

1.3 X-Ray Diffraction

X-Ray Diffraction (XRD) is a measurement technique used to study the phase and lattice parameters of a crystal. All XRD measurements are taken using the Rigaku Geigerflex, which uses the Bragg-Brentano geometry and contains a Cobalt anode that produces x-rays of wavelength 1.79Å. Since the wavelength of the x-rays produced are on the order of angstroms, when an x-ray is incident on a crystal, most rays reflect, but some refract. The reflected rays undergo constructive or destructive interference depending on their path length difference, producing a diffraction pattern, and the condition for constructive interference is called Bragg's Law.

1.3.1 Derivation of Bragg's Law

Consider the family of parallel planes in a crystal given by Miller index (hkl), separated by a distance of $\mathrm{d_{hkl}}$, as in Figure 7. Suppose a ray makes an angle of ϑ with respect to the planes, and let $\vec{\mathrm{n}}$ denote the vector normal to these planes, called the diffraction vector. At each layer, most of the ray is refracted, but some is reflected by the plane. The reflected rays interfere either constructively or destructively depending on their path length difference. For neighbouring planes, the path length difference of the reflected rays is given by

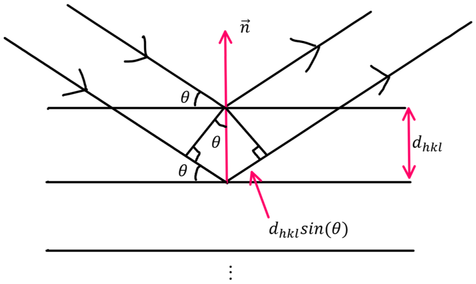

Figure 7: Derivation of Bragg Law

$$\Delta \mathrm{r} = 2\mathrm{d}\sin(\vartheta)$$

Constructive interference occurs when $\Delta\mathrm{r} = \mathrm{n}\lambda$, where n is a positive integer. Therefore,

$$\mathrm{n}\lambda = 2\mathrm{d}\sin(\vartheta)$$

Rewriting in terms of $\mathrm{d_{hkl}}$ gives Bragg's law

$$\lambda = 2\mathrm{d_{hkl}}\sin(\vartheta_{\mathrm{hkl}})$$

When the Bragg condition is satisfied, constructive interference occurs, and at that angle ϑ_{hkl}, a peak in the XRD measurement will be observed.

1.3.2 Structure Factor and Intensity

The structure factor is defined as

$$\mathrm{F_{hkl}} = \sum_{\mathrm{j}} \mathrm{f_j N_j e^{2\pi i(hx_j+ky_j+lz_j)}}$$

Where $\mathrm{f_j}$ is the scattering factor, which measures how well a particular atom scatters x-rays, $(\mathrm{x_j, y_j, z_j})$ is its position, and $\mathrm{N_j}$ is the fraction that the atom occupies in that position. As an example, NiO has an fcc lattice, and its basis is a $\mathrm{Ni^{2+}}$ ion paired with an $\mathrm{O^{2-}}$ ion. To find the structure factor of the NiO lattice, it is useful to first determine the structure factor of an arbitrary fcc lattice.

In the fcc lattice, there are 4 distinct positions that the atom can take. In atomic coordinates, these positions are $(0, 0, 0)$, $(\frac{1}{2}, \frac{1}{2}, 0)$, $(\frac{1}{2}, 0, \frac{1}{2})$ and $(0, \frac{1}{2}, \frac{1}{2})$. Thus, the structure factor is

$$\mathrm{F_{hkl}} = \mathrm{f(e^0 + e^{i\pi(k+l)} + e^{i\pi(h+l)} + e^{i\pi(h+k)})}$$

Which simplifies to

$$\mathrm{F^{fcc}_{hkl}} = \begin{cases} \mathrm{4f} & \mathrm{(h, k, l)\,all\,even\,or\,all\,odd} \\ 0 & \mathrm{(h, k, l)\,mixed} \end{cases}$$

The NiO lattice can also be thought of as an fcc lattice made of $\mathrm{Ni^{2+}}$ combined with an fcc lattice made of $\mathrm{O^{2-}}$, where the $\mathrm{O^{2-}}$ lattice is shifted by $(\frac{1}{2}, \frac{1}{2}, \frac{1}{2})$. Therefore, its structure factor is just the sum of the structure factors of the individual lattices, taking into consideration that the $\mathrm{O^{2-}}$ lattice is offset by $(\frac{1}{2}, \frac{1}{2}, \frac{1}{2})$.

$$\mathrm{F_{hkl}} = \mathrm{F^{Ni}_{fcc}} + \mathrm{e^{-i\pi(h+k+l)}F^{O}_{fcc}}$$

Where $\mathrm{F_{fcc}}$ is the structure factor of the fcc lattice, and $\mathrm{e^{-i\pi(h+k+l)}}$ is an extra factor to account for the offset of the O lattice. The formula simplifies to

$$F_{hkl}^{NiO} = \begin{cases} 4(f_{Ni} + f_O) & (h,k,l)\,\text{all even} \\ 4(f_{Ni} - f_O) & (h,k,l)\,\text{all odd} \\ 0 & (h,k,l)\,\text{mixed} \end{cases}$$

Due to the symmetry of a crystal, as modeled by its structure factor, some families of planes that satisfy the Bragg condition do not produce peaks in the XRD data. This is because the intensity of the reflections of the (hkl) planes, denoted I_{hkl}, is proportional to the magnitude-squared of the structure factor

$$I_{hkl} \propto |F_{hkl}|^2$$

Returning to the NiO example, the family of planes with index $(1,1,1)$ produces a peak, but $(1,0,1)$ does not, as the former is comprised entirely of even integers, while the latter is mixed.

1.3.3 XRD Apparatus

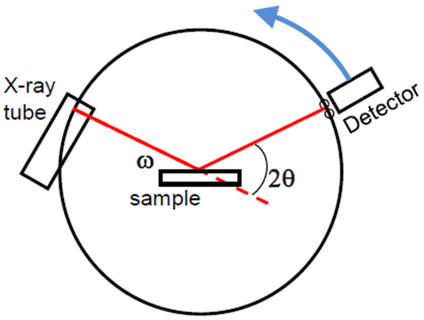

Figure 8: XRD Apparatus, taken from [7]

A simplified XRD apparatus in the Bragg-Brentano geometry is shown in Figure 8, consisting of an x-ray tube, a sample holder and a detector. In the Bragg-Brentano geometry, the x-rays are incident on the sample at an angle of ω, and the detector is located at 2ϑ with respect to the refracted ray. In theory, $\omega = \vartheta$, but due to poor sample orientation and imperfections in the machine, ω will differ from ϑ by a small amount. In the geometry, both ϑ and 2ϑ are changed by rotating the sample and the detector respectively. The detector measures the intensity of the reflected x-ray, in counts, and reports the data as intensity vs. 2ϑ.

The x-rays are produced by striking a target material, called the anode, with a beam of electrons. Electrons with energy greater than the ionization energy of the atoms in the anode will produce photons via the photoelectric effect. The electron in the lower shell of the atom is emitted, and a higher energy electron drops to make the atom stable. In this process, a photon is emitted, and the wavelength of the photon depends on the anode material. In the Rigaku Geigerflex, the x-ray tube uses a cobalt anode, which produces x-rays with wavelength 1.79Å.

1.3.4 XRD of Single Crystals

A single crystal refers to a crystalline sample in which every crystal is oriented in the same direction. To observe a peak in the XRD data, the planes that produce a peak must be properly aligned with respect to the incident x-rays. In other words, the diffraction vector of the planes must be co-linear to the line located between the incident and reflected ray. As in Figure 9, the (011) planes would fail to produce a peak in the XRD data as the diffraction vector $\vec{n}$ is not co-linear to the vector between the incident and reflected ray.

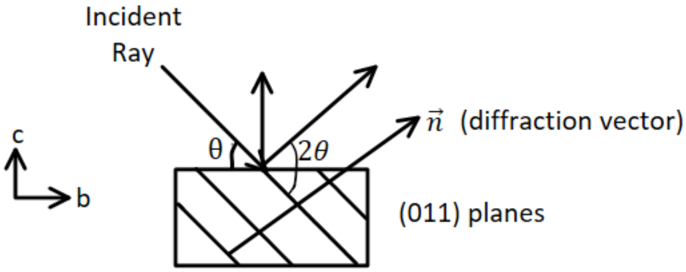

Figure 9: The (011) planes fail to diffract. Diagram based on [7].

As an example, $SrTiO_3$ has a cubic structure, with lattice parameter a = 3.91Å. Suppose that $SrTiO_3$ is placed in the (001) orientation, meaning the ab-axis is parallel to the sample holder. In this case, the only planes properly aligned to produce a peak in the XRD data have index (00l). The first peak corresponds to (001), which has an interplanar spacing of $d_{001} = a = 3.91$Å. For a

Co anode, which emits x-rays of wavelength 1.79Å, the angle of the peak occurs at

$$2\vartheta = 2\arcsin\left(\frac{1.79\text{Å}}{(2)\,(0.391\text{Å})}\right) = 26\,\text{deg}$$

. The next peak corresponds to (002), and is observed at angle $2\vartheta = 54\,\text{deg}$.

1.3.5 Powder XRD

A crystallite is a material made of a single-crystal, in a larger poly-crystalline structure. The ideal sample for powder XRD contains thousands of crystallites in random orientation. When x-rays are incident on a poly-crystalline sample, every crystallite contributes to the diffraction pattern. Suppose an x-ray is incident on a poly-crystalline sample, as in Figure 10. Also, assume that at angles ϑ_1 and ϑ_2, the Bragg condition is satisfied. Some crystallites in the sample will diffract when x-rays are incident at angle ϑ_1, and due to their random orientation, some might produce a reflected ray at various azimuthal angles. Therefore, the ϑ_1 reflection is a cone with an angle $2\vartheta_1$. The same treatment can be done for the ϑ_2 reflections, which corresponds to another cone of angle $2\vartheta_2$. More generally, the diffraction pattern in powder XRD is a series of rings, called the Debye-Scherrer rings.

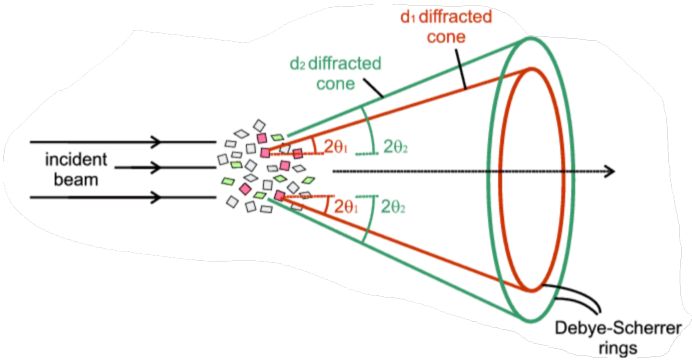

Figure 10: Powder XRD and Debye-Scherrer Rings, taken from [7]

Whereas single-crystal XRD only displays peaks that are properly oriented with respect to the incident x-ray, powder XRD produces all possible diffraction peaks. The assumption that the polycrystalline sample contains thousands of randomly oriented crystallites ensures that there is always some fraction of these crystallites with the right orientation to reflect x-rays towards the detector. In the Bragg-Brentano geometry, the detector only measures one point on each of the Debye-Scherrer rings.

1.3.6 Rietveld Refinement

In this project, an open source software called MAUD is used to fit the XRD data. MAUD performs Rietveld Refinement, a non-linear curve fitting method.

1.4 Atomic Force Microscopy

Atomic Force Microscopy (AFM) is used to measure the topography of a sample, and in this experiment, it is used to deduce the thickness of the thin film samples, In AFM, a cantilever is run across the surface of the sample. A laser is reflected off of the cantilever, and the intensity of the reflected beam is measured using a photodiode. By determining the deflection of the cantilever, the topography of the sample can be found.

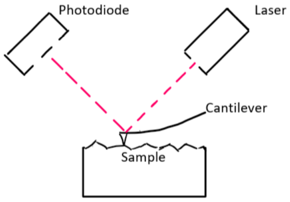

Figure 11: AFM Apparatus

1.5 Resistance vs. Temperature Measurements

Resistance vs. Temperature measurements are taken using the four probe method. 4 lines are drawn on the sample using silver paint, as in Figure 12. The outer lines correspond to current, and the inner lines correspond to voltage. Current is driven through the sample, and the voltage drop is measured across the inner lines. In the two-probe method, resistance is measured with an

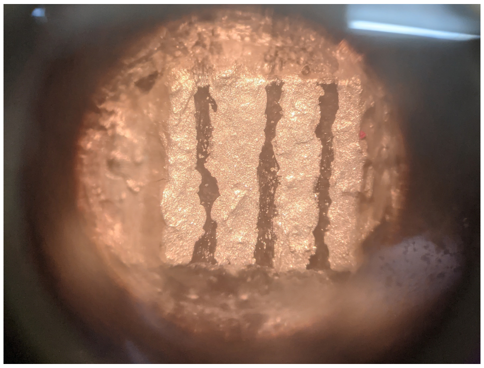

Figure 12: Four lines of silver paint drawn on thin film sample.

Ohmmeter directly. This is problematic as the internal resistance of the wires, and resistance at the contact of the wires and the sample, affects the measurement. Since current is not driven through the voltage probes in the four-point method, these effects do not occur, improving the accuracy of the measurement.

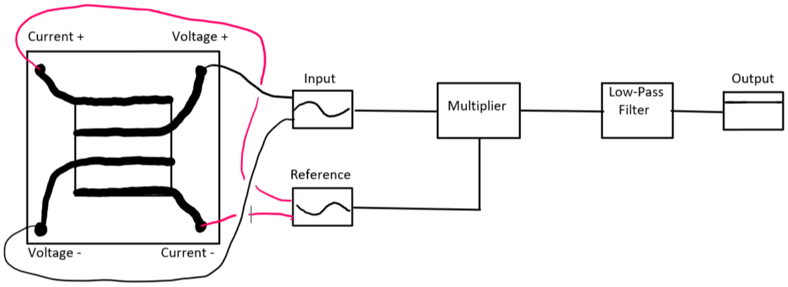

Figure 13: Schematic of Lock-In Amplifier

In this experiment, a lock-in amplifier is used to take the resistance measurements, a schematic of which is given in Figure 13. In general, a lock-in amplifier uses the orthogonality of sinusoidal functions to deduce a measurement that is buried in noise. A current is applied across the sample with a known frequency ω_{ref} and amplitude I_0, and the voltage is measured in response. The reference signal is a sinusoidal wave with same frequency as the applied current, and can be written as

$$\mathrm{V}_{\mathrm{ref}} = \sin(\omega_{\mathrm{ref}}\mathrm{t})$$

. The measured voltage signal is of form

$$V_{\mathrm{sig}} = V_0 \sin(\omega t + \varphi)$$

where φ is an arbitrary phase. The multiplier takes the measured voltage signal and multiplies it with the reference signal, giving an alternating voltage of form

$$V_{\mathrm{multiplied}} = \frac{1}{2} V_0 \cos((\omega_{\mathrm{ref}} - \omega_{\mathrm{sig}})t + \varphi) - \frac{1}{2} V_0 \cos((\omega_{\mathrm{ref}} + \omega_{\mathrm{sig}})t + \varphi)$$

The signal is a mixture of two alternating voltages, one with frequency $\omega_{\mathrm{ref}} + \omega_{\mathrm{sig}}$ and the other with frequency $\omega_{\mathrm{ref}} - \omega_{\mathrm{sig}}$. In the last step, the signal is passed through a low-pass filter, set to only allow DC signals through. The output is nothing, unless $\omega_{\mathrm{ref}} \approx \omega_{\mathrm{sig}}$, in which case the output is

$$V = \frac{1}{2} V_0 \cos(\varphi)$$

Through this process, the value of V_0 can be extracted from noise.

Once the voltage is measured, the resistance of the sample is given by Ohm's law, $R = \frac{V}{I}$. The resistivity can be calculated using $\rho = \frac{RA}{l}$, where A is the cross-sectional area of the sample, and l is its length. Letting d denote the distance between the voltage contacts, t be the thickness of the sample, and L the sample length, the resistivity is

$$\rho = \frac{L}{d} R t$$

Assuming the voltage and current contacts are equidistant, $\rho \approx 3Rt$.

1.6 Furnaces and High-Pressure Furnace

Most solid state reactions in this experiment are done in a Carbolite high-temperature furnace, which can reach a maximum temperature of 1500 °C. To synthesize $Pr_{0.8}Sr_{0.2}NiO_3$ in bulk, a high-pressure furnace is used, which can safely reach a maximum temperature of 900 °C. The high-pressure furnace is connected to an external oxygen supply which can fill the furnace to a maximum pressure of 150 bar at room temperature.

The temperature of the furnaces is measured using a thermocouple. A thermocouple consists of two wires, made of different metals, joined at two junctions. The reference junction is placed at a known temperature, such as an ice bath or room temperature, and temperature is measured at the measurement junction. Thermocouples operate on the principle of the Seebeck Effect. In the Seebeck Effect, when a temperature gradient is applied to a metal, free electrons on the hotter end travel to the cooler end. This produces a potential difference given by $V = S(T_1 - T_2)$, where S is the Seebeck Coefficient, which depends on the material of the metal. In a thermocouple, when a temperature gradient is present, the same process occurs, leading to a potential difference in both metals. However, since different metals are used, they also have different Seebeck coefficients, which produces a nonzero net potential difference between the wires at the voltmeter. The potential difference depends on the temperature of the reference and measurement junctions, enabling one to measure the temperature at the measurement junction.

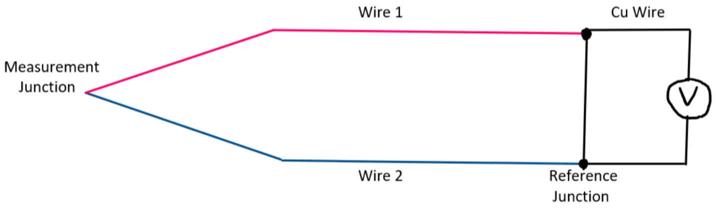

Figure 14: Thermocouple

1.7 Pulsed Laser Deposition

Pulsed Laser Deposition (PLD) is a technique used to produce thin films. The general apparatus consists of a laser, a focusing lens and a PLD chamber.

A laser is used to strike the target, vapourizing the top layer of the target. The vapourized material forms a plasma known as a plume. The plume deposits on the substrate epitaxially, meaning the crystal grows in the same orientation, based on the orientation of the substrate.

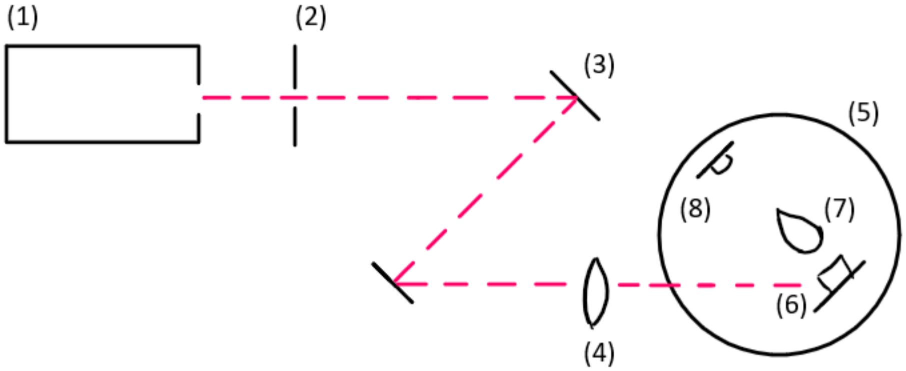

Figure 15: Apparatus for Pulsed Laser Deposition. (1) 248 nm KrF Excimer Laser, (2) Slit (1.2 cm x 0.5 cm), (3) Lenses for reflection, (4) Convex lens, (5) PLD Chamber, (6) Target holder and target, (7) Plume, (8) Substrate heater and substrate

1.7.1 PLD Chamber

The PLD chamber contains a polycrystalline sample of the thin film, called the target, and a substrate, which the thin film grows on top of. The substrate can be heated using a substrate heater. The PLD chamber is often put under high vacuum, but oxygen can be added to the chamber to ensure the thin film samples are fully oxygenated after synthesis.

The PLD chamber used in this experiment can reach pressures as low as 1×10^{-5} torr. As well, the substrate heater can safely maintain a maximum temperature of 900 °C. A convex lens focuses the incident laser to a spot size of approximately 2.0 mm x 1.5 mm.

1.7.2 Ion Gauge

At low pressures, below 10^{-3} torr, an ion gauge is used to measure the pressure of the chamber. An ion gauge consists of a filament, a helical grid and a collector. The filament is heated, which causes it to release electrons. The electrons are attracted to a positively charged grid. Most electrons pass through the grid and ionize gas molecules in the volume of the ion gauge. These ionized gas molecules are attracted to the negatively charged collector located at the centre of the grid. A current is generated, and this current is proportional to pressure of the gas, enabling the pressure to be determined.

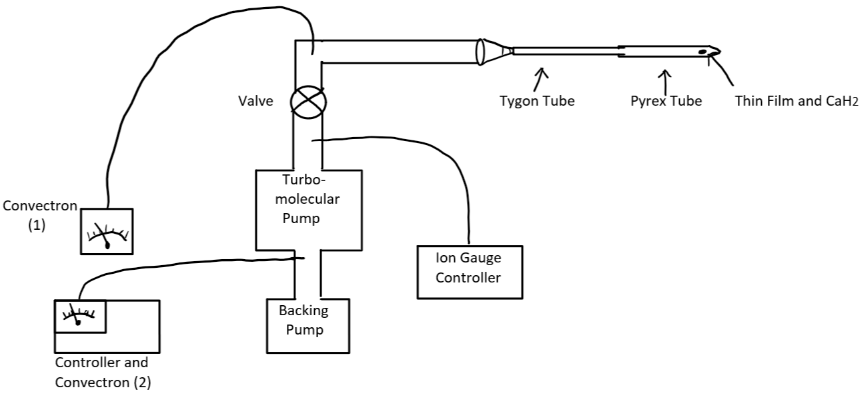

Figure 16: Reduction Apparatus

1.7.3 Laser

In this experiment, a 248 nm KrF excimer laser, manufactured by Lambda Physik, is used to strike the target. Since 248 nm is on the UV spectrum, and is thus not visible to the eye, a white light is also emitted to represent the location of the laser, but this light is quite faint.

In general, the KrF laser works as follows. The gas consists of Kr and F_2 in gaseous state. A potential difference is applied between two electrodes, causing electrons to flow between the gas. These electrons excite the gas molecules, leading to the creation of KrF. Since the KrF molecule is highly unstable, it disassociates back to Kr and F_2. The disassociation leads to a discharge of a photon with wavelength 248 nm.

1.8 Reduction Apparatus

The reduction apparatus consists of a turbomolecular pump, devices used to measure pressure, a Pyrex glass tube and a MAPP blowtorch, as shown in Figure 16.

A turbomolecular pump is used to pump the Pyrex glass tube to a vacuum of less than 0.1 mtorr. The exhaust of the pump is connected to a backing pump, which is a less powerful mechanical pump used to ensure that the apparatus operates efficiently. A valve is placed between the turbomolecular pump and the Pyrex tube, which can be quickly closed if the glass tube breaks.

There are two convectron pressure gauges and an ion gauge in the apparatus. The first convectron gauge is located between the turbomolecular pump and the backing pump, and has a range of 0.1 torr to 0.001 torr. The second convectron gauge is located between the the valve and the Pyrex tube, with a range of 0.1 torr to 0.0001 torr.

2 Experiment 1

2.1 Synthesis of Target

The precursors Nd_2O_3. NiO and $SrCO_3$ were ground in a mortar and pestle in the stoichiometry of $Nd_{0.8}Sr_{0.2}NiO_3$. The ground powder was then reacted in a furnace at 1200 °C for 24 hours, with a ramp-up rate of 300 °C/hour, and furnace cooled to room temperature. The resultant powder was ground and reacted at 1350 °C for 24 hours, using a ramp-up rate of 300 °C/hour. The reacted powder was immersed in isopropyl alcohol and ground for approximately 30 minutes, after which it was pressed into a 2 cm pellet using a hydraulic press. The press pressure used was 4500 psi and the hydraulic press' head has a diameter of 35 mm.

This procedure produces a mixed phase target of $Nd_{1.6}Sr_{0.4}NiO_4 + NiO$ in the stoichiometry of $Nd_{0.8}Sr_{0.2}NiO_3$, via the following reaction

$$4Nd_2O_3 + 2SrCO_3 + 6NiO + \frac{1}{2}O_2 \rightarrow 5Nd_{1.6}Sr_{0.4}NiO_4 + NiO + 2CO_2$$

Once the target is pressed into a pellet, its thickness is measured to be 0.4 cm and its mass is 6.9926 g. Thus, the density of the target is $5.56\frac{g}{cm^3}$. In the mixed phase $Nd_{1.6}Sr_{0.4}NiO_4 + NiO$ target, a stoichiometry calculation shows that 84% of the target is $Nd_{1.6}Sr_{0.4}NiO_4$ by mass, and the remaining 16% is NiO. Using the theoretical densities of $Nd_{1.6}Sr_{0.4}NiO_4$ and NiO found in Section 1.2, the theoretical density of the target can be found via a weighted sum

$$\rho_{\text{theory}} = (7.26\frac{g}{cm^3})(0.84) + (6.84\frac{g}{cm^3})(0.16) = 7.19\frac{g}{cm^3}$$

So, the ratio of the density of the target to its theoretical density is 77%. Since Li et al. were able to produce high quality $Nd_{0.8}Sr_{0.2}NiO_3$ thin films using a target with density 75% [2], the density of the target produced in this experiment should not hinder the growth process.

2.2 Synthesis of Thin Films

Using the $Nd_{1.6}Sr_{0.4}NiO_4$ + NiO target, PLD was used to grow two $Nd_{0.8}Sr_{0.2}NiO_3$ thin films. The PLD chamber was pumped down to a pressure of 5.5×10^{-5} torr, and oxygen gas was added to a pressure of 150 mtorr. The samples were grown on 0.5 mm thick $SrTiO_3$ substrate, which was cut to a size of 2.5 mm x 2.5 mm before the growth. The growth was done using a substrate temperature of 600 °C, using 2000 pulses at a laser frequency of 5 Hz and a laser fluence of 2 J/cm^2. The grown sample was cooled to room temperature at a rate of 15 °C/min to ensure that the films were fully oxygenated.

To find the thickness of the films, one sample was etched in 10% HCl. Half of the film was covered in tape, and the film was then immersed in HCl for 5 seconds. The tape was removed and the film was cleaned using ethanol. As seen in Figure 17, which shows the film after etching, HCl successfully removed the grown film on the uncovered side. AFM was used to measure the topography of the film at the location where etching was done, allowing its thickness to be measured.

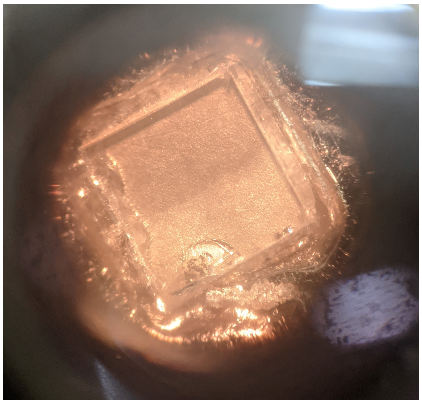

Figure 17: Film after Etching

2.3 Reduction of Thin Films

CaH_2 reduction was used to convert the $Nd_{0.8}Sr_{0.2}NiO_3$ film to $Nd_{0.8}Sr_{0.2}NiO_2$. A 20 inch test tube was sealed on one end using a MAPP blowtorch. Once the test tube cooled to room temperature, the $Nd_{0.8}Sr_{0.2}NiO_3$ thin film was loosely wrapped in aluminum foil and placed at the sealed end of the test tube. Approximately 0.1 g of CaH_2 was also placed at the sealed end of the test tube. The open end of the test tube was attached to the turbomolecular pump apparatus described in Section 1.8 and pumped down to a pressure of 6×10^{-5} torr. After pumping, the tube was sealed with a blowtorch, and its length was measured to be approximately 14 inches. The sealed tube was placed in a furnace at 280 °C for 2 hours, using heating and cooling rates of 10 °C/min. Care was taken to ensure that the CaH_2 powder was not kept in moist air for a long time, as it was observed that CaH_2 reacts with the moisture in the air quickly. The test tube length of 20 inches was chosen to ensure that during the sealing process, heat from the blowtorch does not cause the CaH_2 to prematurely react with the film. As well, this length was selected to prevent the blowtorch from melting the Tygon tubing, which has a melting point of 300 °C. During the sealing process, there was concern that air might be introduced into the tube, causing the pressure inside to exceed 0.1 mtorr. However, no pressure spikes were observed on the convectron gauge, which has a measurement range of 0.1 torr to 0.0001 torr.

3 Experiment 2

The precursors Pr_6O_{11}, NiO and $SrCO_3$ were ground in a mortar and pestle in the stoichiometry of $Pr_{0.8}Sr_{0.2}NiO_3$. The ground powder was reacted at 1200 °C for 24 hours, and then reacted again at 1350 °C for 24 hours, with an intermediate grinding step. The reaction produces mixed phase $Pr_{1.6}Sr_{0.4}NiO_4 + NiO$ in the stoichiometry of $Pr_{0.8}Sr_{0.2}NiO_3$. The mixed phase powder was then reacted in a high pressure furnace at 800 °C for 12 hours. The pressure of the furnace at room temperature was 150 bar, and at 800 °C, the pressure rose to 440 bar. The goal of the high pressure reaction is to convert the mixed phase powder into $Pr_{0.8}Sr_{0.2}NiO_3$ via the following reaction:

$$Pr_{1.6}Sr_{0.4}NiO_4 + NiO + \frac{1}{2}O_2 \rightarrow Pr_{0.8}Sr_{0.2}NiO_3$$

Once $Pr_{0.8}Sr_{0.2}NiO_3$ is synthesized in bulk, the same procedure used to reduce $Nd_{0.8}Sr_{0.2}NiO_3$ films may be repeated to reduce the bulk sample.

4 Results and Discussion

4.1 Experiment 1

4.1.1 XRD of Target

Figure 18 shows the XRD measurements taken of the $Nd_{1.6}Sr_{0.4}NiO_4 + NiO$ target. The possible peaks as a function of 2ϑ are also marked in the figure below the XRD data.

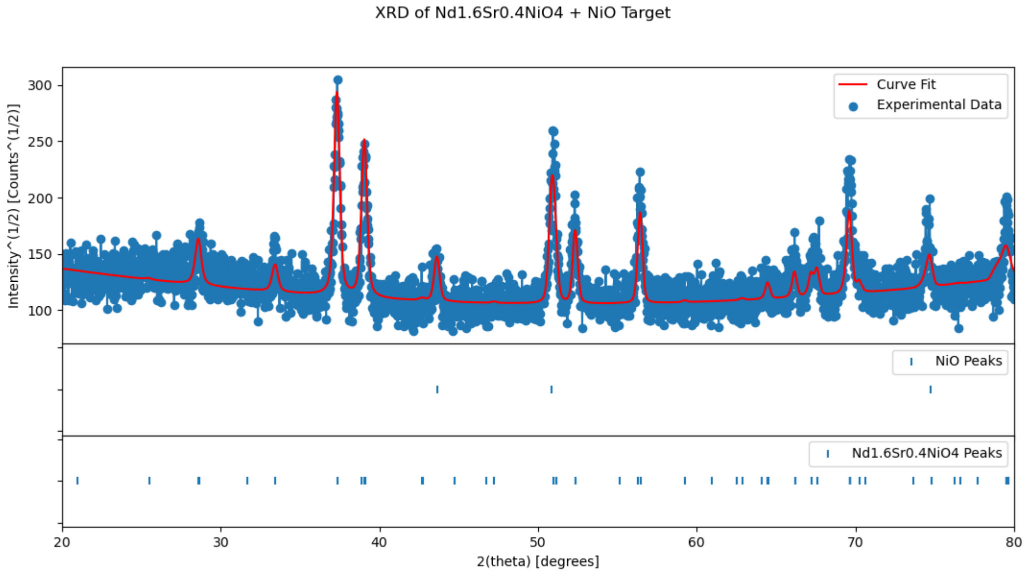

Figure 18: XRD of Target

All peaks in the XRD data correspond to either a $Nd_{1.6}Sr_{0.4}NiO_4$ or a NiO peak, and there are no unexpected peaks. Rietveld refinement is performed on the data, yielding a curve that fits the experimental data well. Therefore, it can be concluded that the target is composed of $Nd_{1.6}Sr_{0.4}NiO_4 + NiO$, and since the precursors were mixed in the stoichiometry of $Nd_{0.8}Sr_{0.2}NiO_3$, the target's stoichiometry must also be the same.

4.1.2 Thickness of Grown Films

The AFM data is shown in Figure 19, and a small box is drawn at the boundary between the etched and un-etched parts of the sample. The distribution of the vertical distances within this box is plotted, which gives Figure 20.

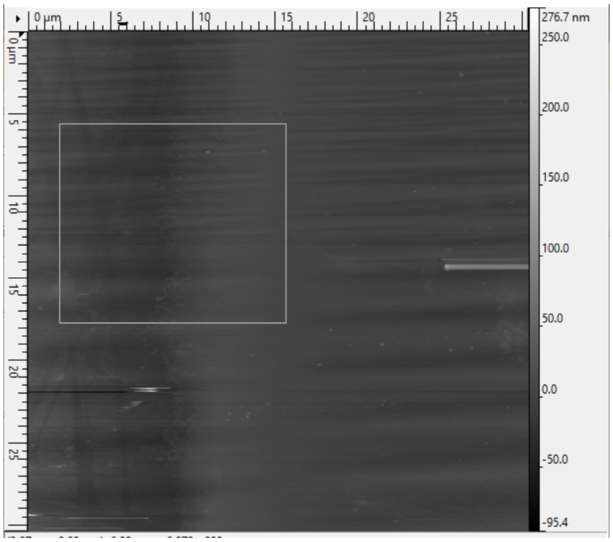

Figure 19: AFM of Etched Film

The distribution contains two peaks at thicknesses of -8 nm and 7 nm. Therefore, the thickness of the grown films is approximately 15 nm.

4.1.3 XRD of Film Post-Growth

Figure 21 shows the XRD data of the film after growth.

As calculated in Section 1.3.4, $SrTiO_3$ oriented in the (001) direction produces two visible

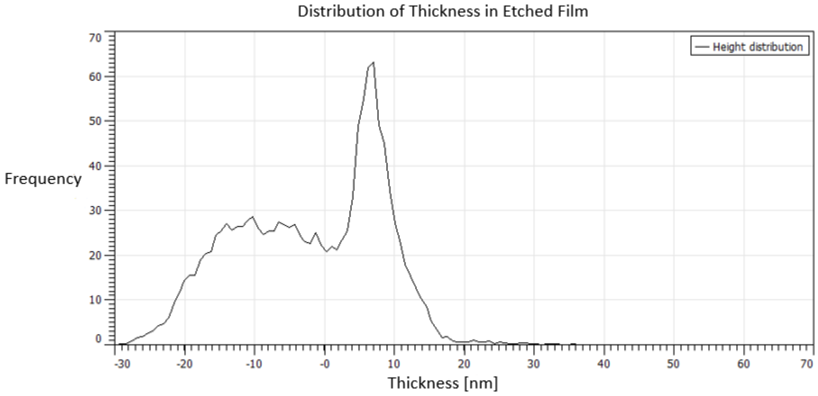

Figure 20: Distribution of Heights of Etched Film

peaks. The first peak, corresponding to the (001) planes, occurs at $2\vartheta = 26°$. The (002) peak occurs at $2\vartheta = 54°$. In Figure 21, there are peaks at 27 and 54 degrees, which can be attributed to the $SrTiO_3$ substrate.

Li et al. grew $Nd_{0.8}Sr_{0.2}NiO_3$ on $SrTiO_3$, at a thickness of 11 nm. In their XRD data, displayed in [1], they observe $Nd_{0.8}Sr_{0.2}NiO_3$ peaks at approximately $2\vartheta = 24°$ and $2\vartheta = 49°$, using a Cu anode [1]. For a Co anode, this would correspond to peaks at $2\vartheta = 28°$ and $2\vartheta = 58°$ In Figure 21, the peak at 59 degrees corresponds to the (002) planes of $Nd_{0.8}Sr_{0.2}NiO_3$. It is likely that since the (001) peaks are expected to occur at 28 degrees, and $SrTiO_3$ has peaks at 27 degrees, the (001) peaks are just hidden beneath the substrate's peaks.

There is an unexpected peak at 49 degrees. Comparing to the XRD patterns of other Ruddlesden-Popper nickelate thin films, which can be found in [15], the position of the peak corresponds closest to the (006) planes of $Nd_{1.6}Sr_{0.4}NiO_4$.

The lattice parameter of $Nd_{0.8}Sr_{0.2}NiO_3$ can be computed using its the XRD data obtained in Figure 21. From Bragg's law, and the fact that $d_{002} = \frac{c}{2}$,

$$\lambda_{Co} = c\sin\left(\frac{59°}{2}\right)$$

The c-axis lattice parameter of $Nd_{0.8}Sr_{0.2}NiO_3$ is $c = 3.64Å$, which is smaller than the bulk

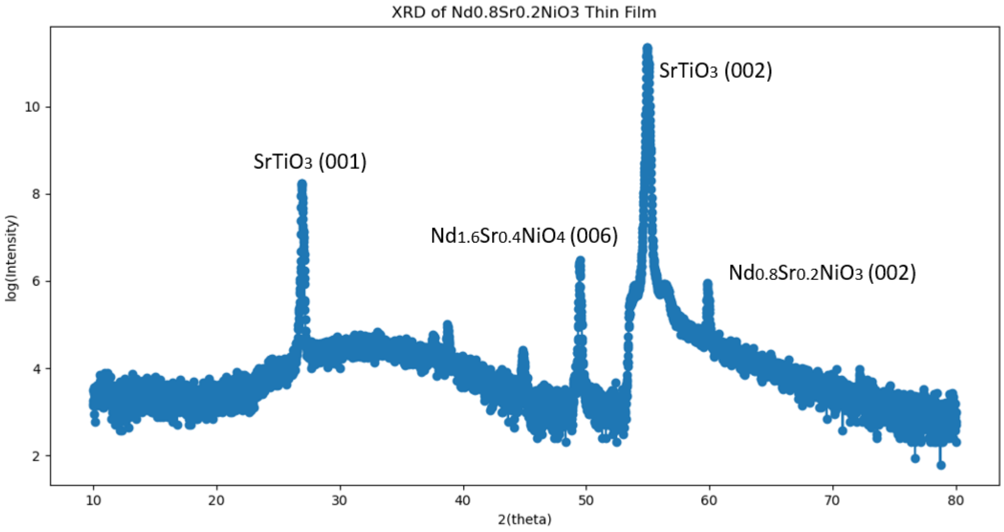

Figure 21: XRD of the Grown Film

pseudocubic lattice parameter of c = 3.81Å, Therfore, the $Nd_{0.8}Sr_{0.2}NiO_3$ film's c-axis is being compressed due to strain provided by the substrate.

4.1.4 Resistance vs. Temperature of Film Post-Growth

The resistance vs. temperature measurements of the film is shown in Figure 22.

The resistivity is calculated using $\rho = 3Rt$, found in Section 1.5. Figure 23 shows the log-log plot of resistivity vs. temperature, which resembles a linearly decreasing trend.

The resistivity increases as temperature decreases, a property characteristic of insulators. Since $Nd_{0.8}Sr_{0.2}NiO_3$ thin films exhibit metallic behaviour, meaning their resistivity decreases as temperature decreases, it can be concluded that the top layer of the sample is not the $Nd_{0.8}Sr_{0.2}NiO_3$ phase.

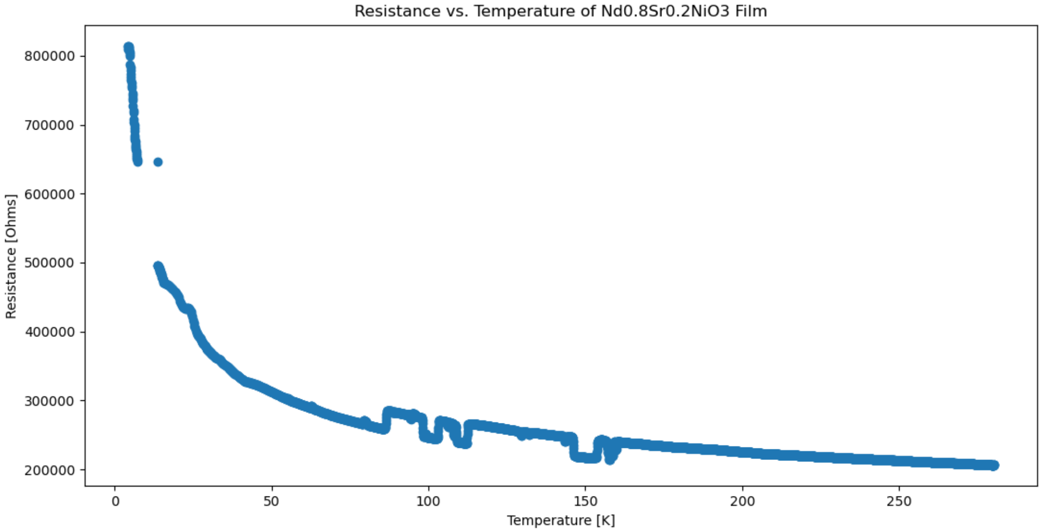

Figure 22: Resistance vs. Temperature of Grown Film

4.1.5 XRD of Film Post-Reduction

The film is reduced via the CaH_2 reduction procedure described in Section 1.8, and the XRD measurement of the resultant film is given in Figure 24.

The peaks at 27 and 54 degrees correspond to the $SrTiO_3$ substrate. However, the peaks observed in the pre-reduced sample are not visible after reduction. As well, no peaks corresponding to $Nd_{0.8}Sr_{0.2}NiO_2$ are visible. The resistance of the sample at room temperature is measured to be 0.94 MΩ.

4.1.6 Discussion

In summary, the XRD data showed that after growth of the $Nd_{0.8}Sr_{0.2}NiO_3$ film, the film contained the $SrTiO_3$ substrate, $Nd_{0.8}Sr_{0.2}NiO_3$ and $Nd_{1.6}Sr_{0.4}NiO_4$. The R vs. T data showed that the sample is insulating, implying that the top surface of the sample is an insulator. Since $Nd_{0.8}Sr_{0.2}NiO_3$ is metallic, and $Nd_{1.6}Sr_{0.4}NiO_4$ is insulating, the sample contains a top $Nd_{1.6}Sr_{0.4}NiO_4$ layer, followed by the $Nd_{0.8}Sr_{0.2}NiO_3$ layer.

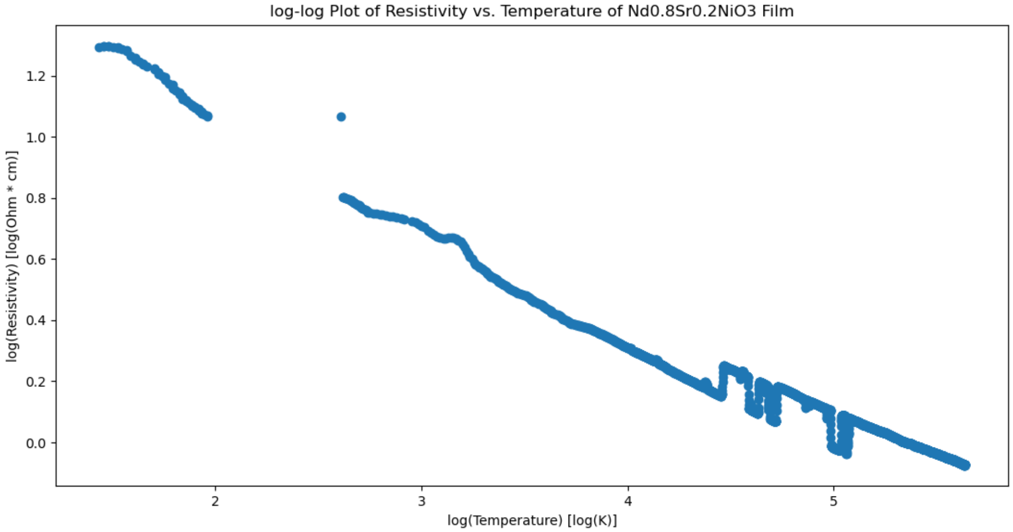

Figure 23: log-log Plot of Resistivity vs. Temperature

Since the XRD pattern of the film after reduction only displays the $SrTiO_3$ peaks, and the resistance of the film at room temperature is $0.94M\Omega$, the grown film likely burned off during the reduction process.

There are two reasons why the $Nd_{1.6}Sr_{0.4}NiO_4$ phase grew instead of the $Nd_{0.8}Sr_{0.2}NiO_3$ phase. As the thickness of the sample increases, the strain provided by the $SrTiO_3$ substrate decreases, increasing the chance for impurity phases to grow in thicker layers. Likewise, the oxygen content in the PLD chamber also plays a role; adding oxygen to the chamber ensures that the sample has stable oxygen content after growth. Since the Ni in the $Nd_{1.6}Sr_{0.4}NiO_4$ phase is in lesser of an oxidation state compared to $Nd_{0.8}Sr_{0.2}NiO_3$, oxygen must be provided to the $Nd_{1.6}Sr_{0.4}NiO_4$ to convert it to the $Nd_{0.8}Sr_{0.2}NiO_3$ phase. Therefore, a lack of oxygen gas in the PLD chamber may have played a role in the growth of the impurity phase, as opposed to $Nd_{0.8}Sr_{0.2}NiO_3$.

To ensure that only $Nd_{0.8}Sr_{0.2}NiO_3$ grows during PLD, a future student can grow thinner films, use a higher oxygen pressure during the PLD process, or grow a $SrTiO_3$ capping layer. As Li et al. discovered, thin films beyond 10 nm in thickness would exhibit impurity phases, so ensuring the thin film thickness is below 10 nm would improve the chances of preventing the growth of the

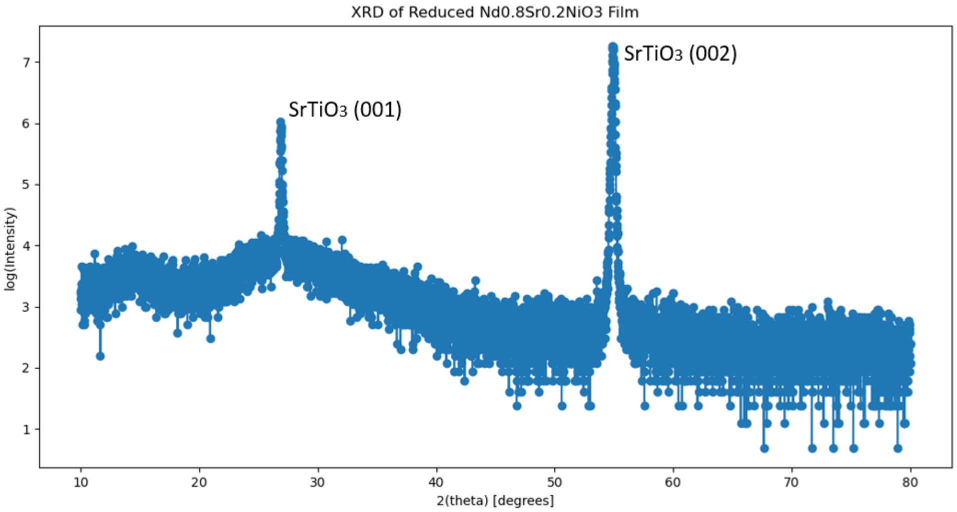

Figure 24: XRD of Film Post-Reduction

$Nd_{1.6}Sr_{0.4}NiO_4$ impurity [2]. Similarly, increasing the oxygen content of the PLD chamber will provide the oxygen gas necessary to promote the growth of the $Nd_{0.8}Sr_{0.2}NiO_3$ phase as opposed to impurity phases. Li et al. also noticed that growing a $SrTiO_3$ capping layer strained the film on both the top and bottom, minimizing the problem of less strain at greater thicknesses, and ensuring that $Nd_{0.8}Sr_{0.2}NiO_3$ grows as opposed to other RP phases.

After reduction, the XRD data only showed the presence of $SrTiO_3$ peaks, and there were no peaks corresponding to $Nd_{0.8}Sr_{0.2}NiO_2$, $Nd_{0.8}Sr_{0.2}NiO_3$, or $Nd_{1.6}Sr_{0.4}NiO_4$. To rule out the possibility that some of thin film remained on the substrate but was amorphous, the resistance of the film was measured at room temperature, and was found to be 0.94 $M\Omega$. Since the resistance of $SrTiO_3$ at room temperature is approximately 1 $M\Omega$, it can be concluded that the film burned off during reduction, and the resulting sample is the $SrTiO_3$ substrate.

To ensure the film does not burn off during reduction, a future student can lower the reduction time or grow a $SrTiO_3$ capping layer. Using a lesser reduction time ensures that the sample is exposed to the reducing agent for lesser time, limiting the chance that the film decomposes during reduction. Growing a capping layer, as observed by Li et al., favours the removal of the apical oxygens as opposed to other oxygens in $Nd_{0.8}Sr_{0.2}NiO_3$, ensuring that the reduction process is

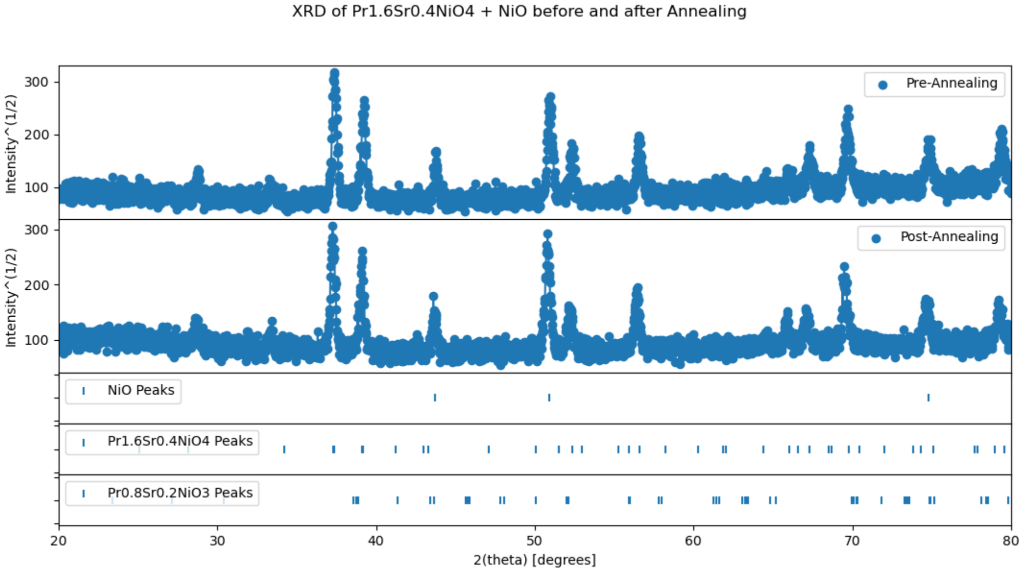

Figure 25: XRD of $Pr_{1.6}Sr_{0.4}NiO_4 + NiO$ before and after Annealing

more controlled [2].

4.2 Experiment 2

4.2.1 XRD

Figure 25 shows the XRD measurements of the sample before and after the high-pressure reaction. Before the high-pressure reaction, every peak can be matched with either a NiO or $Pr_{1.6}Sr_{0.4}NiO_4$ peak, and there are no unexpected peaks, meaning that the powder is $Pr_{1.6}Sr_{0.4}NiO_4 + NiO$. After the high-pressure reaction, the XRD pattern does not change, meaning that a negligible amount of $Pr_{1.6}Sr_{0.4}NiO_4 + NiO$ was converted into $Pr_{0.8}Sr_{0.2}NiO_3$.

As seen, after high pressure reaction, $Pr_{1.6}Sr_{0.4}NiO_4$ remained in the same phase. A future student can produce the $Pr_{0.8}Sr_{0.2}NiO_3$ phase by reacting the sample more times, with intermediate grinding steps. The grinding steps ensures the grain size is smaller, increasing reactivity. As well, performing the reaction multiple times may facilitate the slow transition from the $Pr_{1.6}Sr_{0.4}NiO_4$ to the $Pr_{0.8}Sr_{0.2}NiO_3$ phase.

References

[1] D. Li, K. Lee, B. Y. Wang, M. Osada, S. Crossley, H. R. Lee, Y. Cui, Y. Hikita, and H. Y. Hwang, ”Superconductivity in an infinite-layer nickelate”, Nature 572, 624 (2019), https://doi.org/10.1038/s41586-019-1496-5.

[2] K. Lee, B. H. Goodge, D. Li, M. Osada, B. Y. Wang, Y. Cui, L. F. Kourkoutis, and H. Y. Hwang, ”Aspects of the synthesis of thin film superconducting infinite-layer nickelates”, APL Materials 8, 041107 (2020), https://doi.org/10.1063/5.0005103.

[3] Li, Q., He, C., Si, J. et al. ”Absence of superconductivity in bulk Nd1-xSrxNiO2”, Commun Mater 1, 16 (2020), https://doi.org/10.1038/s43246-020-0018-1.

[4] M, Osada, B. Y. Wang, et al. ”A Superconducting Praseodymium Nickelate with Infinite Layer Structure”, Nano Letters 2020 20 (8), 5735-5740, 10.1021/acs.nanolett.0c01392.

[5] Danfeng Li describes synthesis/electronic structure of nickelate superconductors (FLEET seminar) (https://www.youtube.com/watch?v=-mbEJ7VBo4U)

[6] Kittel, Charles. Introduction to Solid State Physics. 8 ed. John Wiley and Sons. 2005.

[7] http://prism.mit.edu/xray/documents/1%20Basics%20of%20X-Ray%20Powder%20Diffraction.pdf

[8] https://www.thinksrs.com/downloads/pdfs/applicationnotes/AboutLIAs.pdf

[9] Physics Department. “Building and Calibrating a Thermocouple”. Lab manual. 2016. University of Toronto. Toronto. Canada.

[10] Bednorz, J.G., Müller, K.A. Possible highT c superconductivity in the Ba-La-Cu0O system. Z. Physik B - Condensed Matter 64, 189-193 (1986). https://doi.org/10.1007/BF01303701.

[11] Tung, IC., et al. Connecting bulk symmetry and orbital polarization in strained RNiO3 ultrathin films, Phys. Rev. B 88, 205112. https://doi.org/10.1103/PhysRevB.88.205112.

[12] Diao, Chien-Chen & Huang, Chun-Yuan & Chen, Chen-Yi & Wu, Chia-Ching. (2020). Morphological, Optical, and Electrical Properties of p-Type Nickel Oxide Thin Films by Nonvacuum Deposition. Nanomaterials. 10. 636. 10.3390/nano10040636.

[13] A.A. Bassou, et al. Thermal stability and decomposition kinetics of NdNiO3-d at 1 bar of O2, Materials Today Communications, Volume 28, 2021, 102663, https://doi.org/10.1016/j.mtcomm.2021.102663.

[14] Ph. Lacorre, Passage from T-type to T'-type arrangement by reducing R4Ni3O10 to R4Ni3O8 (R = La, Pr, Nd), Journal of Solid State Chemistry, Volume 97, Issue 2, 1992, Pages 495-500, ISSN 0022-4596, https://doi.org/10.1016/0022-4596(92)90061-Y.

[15] https://arxiv.org/ftp/arxiv/papers/2106/2106.12941.pdf

[16] Osada, M., Wang, B.Y. et al. Nickelate Superconductivity without Rare-Earth Magnetism: (La,Sr)NiO2. Adv. Mater. 2021, 33, 2104083. https://doi.org/10.1002/adma.202104083